Thin–Walled Structures 149 (2020) 106614

Contents lists available at ScienceDirect

Thin-Walled Structures

journal homepage: http://www.elsevier.com/locate/tws

Full length article

Crushing of steel tubes with different infills under partial axial loading

Tohid Ghanbari-Ghazijahani, PhD [a,*], Amin Nabati [b], Mojtaba Gorji Azandariani [c], Nader Fanaie, PhD [d]

[a] School of Civil, Environmental & Mining Engineering, The University of Adelaide, SA, 5005, Australia
[b] Sahand University of Technology, Tabriz, Iran
[c] Structural Engineering Division, Faculty of Civil Engineering, Semnan University, Semnan, Iran
[d] Department of Civil Engineering, K. N. Toosi University of Technology, Tehran, Iran

ARTICLE INFO

Keywords:
SHS tubes
Concrete-filled and timber-filled steel tube
Partial axial compression
Crushing
Columns
Experiments
Finite element analysis (FEA)

ABSTRACT

Localised/partial loading is seen in many applications in the building and construction industry. This paper aims to study the influence of localised loading in different positions and Loading Coverage Areas (LCAs) for steel columns with concrete and timber infills, and hollow steel tubes. Fifteen tests were carried out in three categories. Structural stability of the specimens was evaluated far into their plastic response up until crushing. The energy absorption of each specimen was quantified and compared with its counterparts of different materials and LCAs. Axial capacity and failure were focused on as well as the strength-to-mass ratio for each specimen. There was a noticeable capacity difference between the side-loaded and mid-loaded specimens of each group indicating the effect of material under loading on the capacity. The side-loaded specimens had a higher interface between the loading element and steel, compared to the mid-loaded specimens. Numerical analysis was also conducted, which yielded a very close consistency of results with the experiments.

1. Introduction

Using multiple materials to achieve optimised composite sections with improved structural performance is on the rise in the construction industry. Higher structural integrity and resilience against earthquake provided by more ductility and energy absorption alongside lower mass are the drivers of using new composite columns in buildings. Concrete-filled steel tubes (CFSTs) are now extensively used in mid- and high-rise buildings. On the other hand environmental considerations become now more and more important than in the past, and so underscore the usage of timber. The recently developed composite columns as concrete- and/or timber-filled steel tubes have shown growing attention due to its promising structural and environmental advantages [1]. Thus, this research aims to look at these structures from a different angle, wherein partial loading is investigated.

The behaviour of steel tubes filled with concrete was explored by many researchers both experimentally and numerically. Han experimentally looked at the axial behaviour of concrete-filled steel tubes with rectangular sections [2]. Constraining factor and the ratio of dimensions were found effective on ductility and axial load capacity. Han et al. tested fifty CFST stub columns with circular and square sections, various steel yield strengths, and width-to-thickness or diameter-to-thickness ratios under axial loading [3]. Results were compared with different codes and a model was proposed to predict the capacity of sections. Du et al. tested rectangular CFSTs to investigate the effects of high-strength steel on the axial capacity [4]. They showed that the standards EC4, AISC 360, GB50936 are inaccurate to be used for high strength steel tubes. Using experimental and numerical modelling, He and Zhao studied the behaviour of circular CFSTs under partial axial loading [5]. Results highlighted the effect of two parameters on the axial capacity including the ratio of concrete to loading element area and the ratio of plastic resistance of steel over concrete. Gou et al. studied the formation of local buckling in hollow and concrete-filled steel tubes experimentally and numerically considering different depth-to-thickness ratios [6]. They concluded that when depth-to-thickness is more than 50, local buckling is required to be considered. Han et al. explored the behaviour of CFSTs under torsion using finite element software and verified their results by experimental data [7]. Through a parametric study, they developed a formula to estimate the torsional strength and moment.

1.1. Timber and concrete as infill

A number of researchers have recently focused on the usage of timber

* Corresponding author and team leader.
E-mail addresses: t.ghanbarighazijahani@adelaide.edu.au, tohid.ghanbari@utas.edu.au, tohidghanbari@gamil.com (T. Ghanbari-Ghazijahani).

https://doi.org/10.1016/j.tws.2020.106614
Received 7 August 2019; Received in revised form 7 January 2020; Accepted 13 January 2020
Available online 17 February 2020

Nomenclature

A_c	Cross-section area of concrete
A_s	Cross-section area of steel tube
ξ	Confinement factor
DI	Ductility index (75% of peak load)
AE	Absorbed energy
$P_{ult.}$	Peak load
$\delta_{0.85}$	Displacement for 85% of peak load at post-peak region
δ_y	Yield displacement $= 1.33 \times \delta_{0.75}$
σ	Stress of confined concrete
ψ	Dilation angel
f_{b0}	Biaxial compressive strength of concrete
μ	Viscosity parameter
f_{ck}	67% of strength (cubic)
f_y	Yield stress of SHS steel tube
$f_c^{'}$	Uniaxial compressive strength of concrete
α	Steel ratio
DIW	Ductility index (75% peak load) over mass
SAE	Specific absorbed energy
PLW	Peak load (axial) over mass
$\delta_{0.75}$	Displacement at 75% of peak load at pre-peak region
h	Height of specimens
ε	Strain of confined concrete
e	Flow potential eccentricity
f_{c0}	Uniaxial compressive strength of concrete
k	Second stress invariant on tensile meridian divided by second stress invariant on compressive meridian

as a core element inside steel tubes and/or combined with concrete in axial members. The reason behind this idea (timber inside concrete) is to reduce the weight of concrete-filled tubes and yet employ the substantial compressive strength that timber provides, which depending upon species, could be equivalent to the strength of a normal-to high-strength concrete. Several examples are described in this paragraph. Reddy and Al-Hassani focused on crushing behaviour of composite sections including steel tubes and wood core [8]. Different deformation modes, higher axial load and energy absorption were achieved. Ghanbari Ghazijahani et al. tested circular steel tubes filled with different cross-sections of timber [9]. Timber together with Carbon Fibre Reinforced Polymer Composites (CFRP) enhanced the axial behaviour, and the axial capacity increased by 146% in comparison with hollow steel tube. Karampour et al. experimentally investigated the structural response of double-skin timber-filled steel tubes as stub columns [10]. Through a parametric study, they found that the ultimate capacity depends predominantly upon the yield of timber in the new composites. Rectangular steel tubes filled with timber and strengthened with CFRP were studied by Ghanbari Ghazijahani et al. [11]. Timber prevented inward buckling and CFRP delayed the onset of outward buckling, which led to an axial capacity increase of bare specimens by around 75%. Ghanbari Ghazijahani et al. reported concrete-timber-filled steel tubes with a softwood infill [1] under axial compression, and double-skin tubes with Oak dowels, Meranti and concrete [12]. Timber reduced the total weight of the specimens and at the same time enhanced the ductility and energy absorption for some specimens, and affected the post-peak response of the columns. Jiao et al. explored the behaviour of high-strength SHS steel tubes filled with concrete and oak timber under axial compression [13]. Replacing concrete with oak resulted in the same axial capacity as fully concrete-filled tubes, both having 60% capacity enhancement compared to SHS steel tubes. Most recently, Nabati, et al. experimentally studied the axial performance of steel tubes filled with concrete and timber with and without CFRP strengthening under compression [14]. Timber core increased the ductility, and energy absorption capacity while decreased the weight and axial capacity, which then rectified by using CFRP.

1.2. Partial loading or eccentricity

Composite columns such as rectangular concrete-filled steel tubes (RCFST), widely used in high-rise buildings, are often loaded partially in different ways in the cross-section area. Thus, non-uniform/partial loading of composite columns (such as concrete-filled steel tubes) has been a research problem for many researchers. Yang and Han experimentally studied RCFSTs and plain concrete specimens under partial axial loading [15]. RCFSTs showed a higher axial bearing capacity and ductility in comparison with the plain concrete. They also proposed a simplified formula for RCFSTs under partial loading. Yang and Han conducted twenty-eight tests for concrete-filled steel tubes (CFST) with various cross-sections (square, rectangular and circular) and load eccentricity ratios [16]. They performed a Finite Element Analysis (FEA) as well, with which they compared and verified their experimental results. Yang and Han explored the axial behaviour and failure modes of CFSTs under partial compression considering the effects of section shape, length-to-diameter ratio, partial loading ratio and top plate thickness [17]. Yang et al. investigated double-skin steel tubs with concrete infill (referred to as CFDST) under partial axial load [18]. Hollow ratio, loading plate's thickness, and partial area ratio were the main parameters that these authors looked at in their research. The specimens under partial loading exhibited stable and ductile behaviour the same as specimens under full axial loading. Zhang et al. numerically studied the effects of various parameters such as the thickness of loading plate, concrete's compressive strength, the yield stress of outer tube, and partial loading area and hollow ratios in CFDSTs [19]. They concluded that the thickness of the end plate had more effect on the behaviour of CFDSTs under partial loading. It was interesting that concrete experienced higher axial capacities in CFDSTs with partial loading in compression with fully loaded models. Li et al. conducted several experiments to study the behaviour of tapered CFDST columns under eccentric axial load [20]. Using *equivalent column* method, they predicted the capacity of CFDSTs under axial eccentric loading. Yuan et al. experimentally and numerically investigated the axial behaviour of CFSTs with longitudinal stiffeners under axial eccentric loading. It appeared that stability and ultimate strength of columns enhanced by using stiffeners [21].

1.3. The aim of this research

There are examples in design and construction of engineering structures where columns experience partial/eccentric loading including, but not limited to, different types of beam-column connections. To the knowledge of the authors, despite the extensive application of concrete-filled steel tubes in civil engineering structures (such as bridges and buildings), timber-filled steel tubes has not been used as structural elements in engineering application. Given the introduction of timber-filled columns in the first author's previous work (e.g. Refs. [1,9,11,13,14]), and also widespread use of CFT and hollow steel sections, this research aims to evaluate the effect of partial loading on three types of columns: **(i)** Square hollow steel tubes (SHS), **(ii)** timber- and **(iii)** concrete-filled steel tubes (STFST and SCFST). Each group of specimens are compared with their counterparts from other groups in terms of infill, location of loading, and Loading Coverage Areas (LCAs). Also, a numerical study was conducted to compare the results of the experiments. The key finding was that, unlike the initial expectations, the

specimens with the loading element at the extreme end of the cross-section, showed the highest axial capacities. Detailed discussions are presented in the coming sections.

2. Instrumentation and experiments

2.1. Setup and tests

Fig. 1 shows different components of the AMSLER machine as the loading system of this experimental program. This machine with 5000 kN capacity, supported both load and displacement control modes of testing. An internally installed load-cell recorded the axial load, while four LVDTs were mounted at every corner of a square loading deck to measure displacements. The displacements were controlled through moving the bottom deck vertically.

A data acquisition system was employed to control and record the load, displacement, time and strain data. Axial displacement was applied with a constant rate after centralising specimens in the middle of the loading plates and adjusting the loading element on the specimen. Five different loading schemes were selected as illustrated in Fig. 2. In general, full and partial loading was adopted. For the partial load, two loading elements with the dimensions of 30 × 30 × 90 mm and 50 × 50 × 90 mm were utilised between the upper loading plate and the specimens. These elements were made of square steel profiles, and due to their sizable thickness, their integrity was not affected under loading. Three-dimensional schematic views of specimens under full and partial axial loading are presented in Fig. 3.

2.2. Materials

Specimens were made of different combinations of steel, concrete and timber. Tensile coupon tests for steel were conducted according to the Australian Standard AS1391 and the results are tabulated in Table 1 and depicted in Fig. 4-a. Four timber samples were cut parallel to the grain and tested under compression according to ASTM-D 143. The results are presented in Table 1 and Fig. 4-b. Standard cylindrical concrete samples were made from the same batch of the concrete used for the specimens, cured in a fog room, and tested after 28 days. The results are tabulated in Table 1.

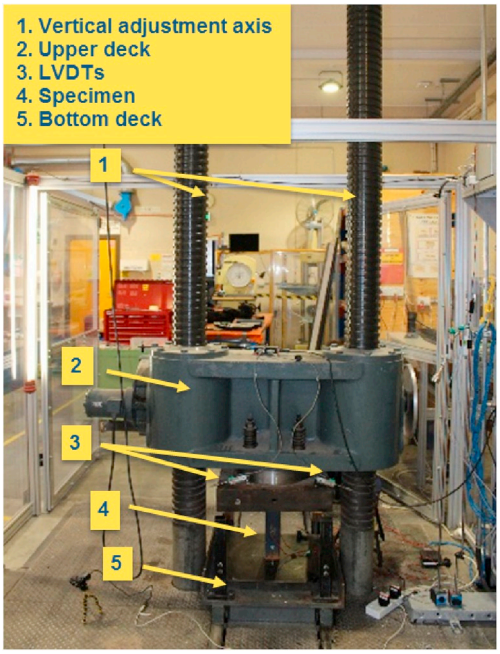

Fig. 1. Test setup and components.

2.3. Specimens and preparation

Three typical sets of specimens were made including hollow steel tubes, steel tubes filled with timber, and concrete. Details of the specimens are presented in Table 2. The steel tubes were SHS sections with the dimensions of 75 × 75 × 5 mm, which were cut and prepared in 300 mm of length. For timber-filled tubes, the timbers were cut, rounded off at corners and inserted in the steel tubes making a moderate amount of friction between steel and timber. To make CFT specimens, the concrete mix was designed, concrete was prepared, and poured inside the tubes at various layers. For each layer, vibration was carried out to ensure high-quality and dense concrete. After curing the concrete for 28 days, two end surfaces of the specimens were flattened to ensure an even distribution of the axial compression whilst loading.

Specimens' label includes two components: **(i)** the main label and **(ii)** a subscript. The labels are HS, TS, and CS representing hollow steel, timber-filled, and concrete-filled steel respectively. The subscripts are composed of a number that presents the width of the loading element and a letter (S for side and M for middle, hereafter called side-loaded and mid-loaded) showing the location of the loading element. Table 3 further describes the labelling method of the specimens.

3. Test results

3.1. Failure modes

Figs. 5–7 show the failure progress of specimens TS_F, CS_{30M}, and TS_{50S}, wherein No.1 on the sub-figures indicates the specimen with no deformation, while No.2 to No.5 show the increments of the deformations. The failure of fully concrete- or timber-filled specimens was the typical failure mode of local plastic buckling as bulging of the steel tube at one end. As loading progressed, buckling lobes were developed one at a time; in the specimen with concrete infill, rupture of the seam of the tube was observed (albeit well-into the plastic region), which led to the concrete be discharged out of the tubes.

For partially loaded tubes, the loading element started penetrating into the specimens, which was accompanied by the onset of nonlinear plastic deformations on the load-displacement graphs. This penetration, on the one hand, led clearly to the shear rupture of the steel, concrete and timber cutting across the height of the loading element. On the other hand this phenomenon was seen along with crushing the timber and concrete (Fig. 8), while steel was concurrently rolled over to the sides as the load increased. For the specimens that the loading element was on the extreme side, as large displacements occurred, the loading element was somewhat slid into the cross-section as the side area of the tube, which was under the loading element, buckled outwards. Nonetheless, for the specimens with the loading elements in the middle of the specimens, a more symmetric failure shape was achieved.

3.2. Load displacement and strain response

Fig. 9 shows the load-displacement behaviour of the fully and partially loaded specimens. As a common feature between all the specimens, the concrete-filled tubes had a more stable post-yield response as the load-carrying capacity of these specimens increased after the yield load. For fully-loaded specimens, timber-filled and hollow tubes had a mild inelastic transition between the yield and the peak load after which the load decreased steadily until termination of the experiment. For partially loaded specimens, the load reduction after the peak load was almost similar for hollow and timber-filled specimens, whilst the concrete-filled tubes experienced an increase after the yield.

The position of strain gauges is shown in Fig. 10. Fig. 11 shows the strain response of the specimens. Two strain gauges (SG2 and 4) were used for each specimen in a way that numbers 2 and 4 represent the number of sides in the cross-sections. SG2 was the only strain gauge that was on a face straight under the loading element for the side-loaded

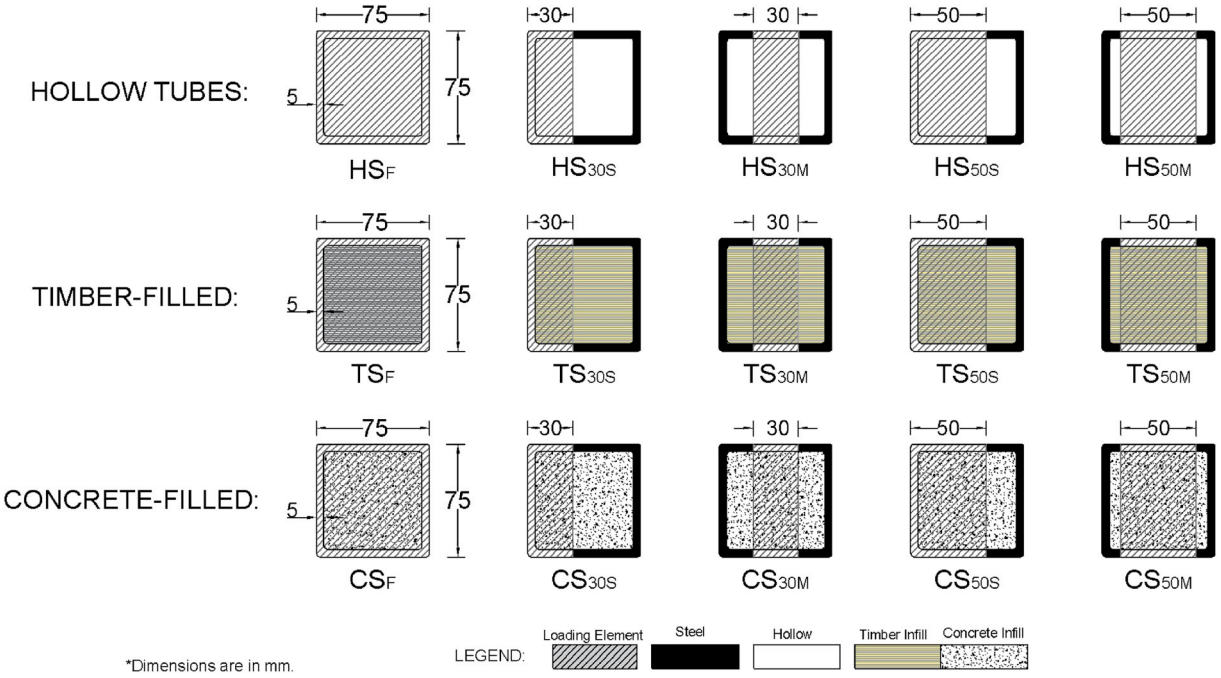

Fig. 2. Cross-sectional view of all specimens.

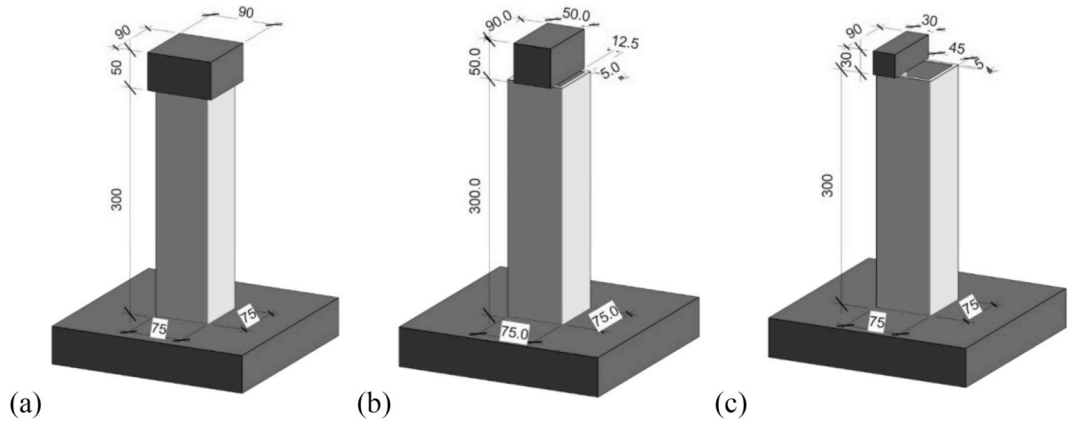

Fig. 3. 3D schematic overview representation of test specimens: (a) HS_F (b) HS_{50M} (c) HS_{30S}.

Table 1
Material properties.

Properties	Steel	Concrete	Timber
Average compressive strength* (MPa)	–	60	40.97
Average modulus of elasticity* (MPa)	189×10^3	364×10^2	4.21×10^3
Yield stress (MPa)	420	–	–
Ultimate stress (MPa)	559	–	–
Poisson's ratio	0.25	0.176	0.30
Density (kg/m^3)	7850	2400	418

Note: *For timbers, parallel to grain values are included.

specimens. SG4, however was away from the loading in the side-loaded specimens, attached to a face opposite side of SG2 (both facing one another).

Due to the location of the strain gauges the strain values for SG2 were higher than SG4 for the side-loaded specimens. It is obvious that SG2 was straight under the partial loading; accordingly axial stress was high for this specimen. It has to be noted that the failure mode of the specimens suggests that the effect of crushing (localised axial deformations) effectively dominated the effect of bending caused by eccentricity for side-loaded specimens. This is due mostly to the total length of the specimens, as the specimens are regarded *stub* columns so the eccentricity cannot cause significant bending stress to trigger overall (column) buckling. Additionally, the eccentricity is applied through a relatively short arm such that the loading element in the side-loaded specimens was still within the geometry of the cross-section. Conversely, a significant eccentricity is expected when the arm is long enough to produce an effective bending, e.g. applied away from the cross-section.

The dominance of the axial deformations to the bending was manifested in the magnitudes of the strains for the side-loaded specimens as SG2 recorded higher values than SG4. For fully loaded and partially but symmetrically loaded (mid-loaded) specimens, the values of the strain gauges were very close to each other verifying the validity of one another. Comparing the strain values of all three types of specimens, the concrete-filled specimens possessed generally higher strain values suggesting that for this particular geometry of the specimens concrete had a better synergy with steel so that higher strains (corresponding to greater loads) were achieved, i.e. higher strain together with higher capacity indicate that (regardless of cost, weight, and environmental

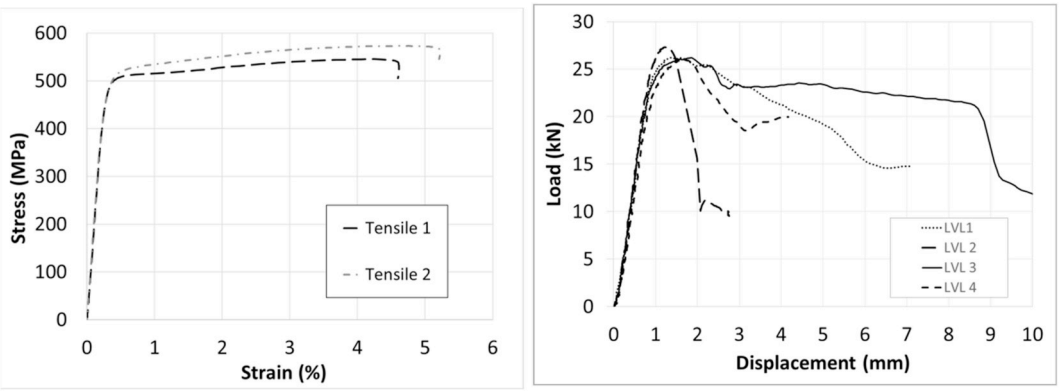

Fig. 4. (a) Stress-strain diagram for steel, (b) Load-displacement response for timber samples.

Table 2
Specifications of specimens.

No.	Specimens	Specimen type	Total mass (kg)	Ultimate strength-experimental (kN)	Strength/mass ratio (kN/kg)
1	HS_F	Hollow Steel Tube	2.99	813.1	271.9
2	HS_{30M}			271.3	90.7
3	HS_{30S}			390.0	130.4
4	HS_{50M}			378.9	126.7
5	HS_{50S}			520.3	174.0
6	TS_F	Timber-Filled Steel Tube	3.52	894.2	254.0
7	TS_{30M}			389.9	110.8
8	TS_{30S}			442.0	125.6
9	TS_{50M}			540.4	207.7
10	TS_{50S}			648.0	194.3
11	CS_F	Concrete-filled Steel Tube	5.93	980.3	165.3
12	CS_{30M}			782.0	131.9
13	CS_{30S}			529.9	89.4
14	CS_{50M}			921.8	155.4
15	CS_{50S}			907.1	153.0

Table 3
Description of components of the specimens' labelling.

Letters in specimens' labels		Subscript			
HS	Hollow steel tube	**-**	–	**F**	Full coverage
TS	Timber-filled steel tube	**30**	Loading element 30 × 30 mm	**M**	Middle
CS	Concrete-filled steel tube	**50**	Loading element 50 × 50 mm	**S**	Side

considerations) the composite of concrete and steel performed better than the other specimens. Despite this though, other parameters – such as total cost, weight (resilience against earthquake), and environmental considerations – may outweigh the capacity, which requires an overarching study to reach definitive conclusions.

3.3. Ultimate axial capacity of specimens under full and partial loading

Among the specimens of each group, specimens under full loading had a higher ultimate load than the partially loaded specimens (Fig. 12-a). It is evident that LCA affects the axial stress and the capacity accordingly, so as LCA increases the stress is distributed in a larger area leading to a capacity rise. Thus, after the fully-loaded specimens, the specimens with a larger loading element (50 × 50 mm) had higher capacities, which followed by specimens with smaller loading elements (30 × 30 mm). It is fitting to note here that, based on the literature, when such composite sections are loaded purely axially, the bond/interaction between different materials (except for confinement effect which is well known to the research community) does not significantly affect the capacity nor the general response of the stub columns.

More importantly, there is a noticeable difference between the side-loaded and mid-loaded specimens of each group, which indicates the effect of material under loading on the ultimate capacity. The side-loaded specimens had a higher interface between the loading element and the *steel*, compared to the mid-loaded specimens. As such, due to the higher compressive strength of steel (especially given that buckling of steel is restrained through infills) compared to the timber and concrete, a higher interface with steel led to a greater capacity.

Comparing hollow with timber-filled specimens under partial loading, timber increased the capacity for all types of loading up to an average value of 30%. This rise is not as significant as concrete-filled specimens (compared to SHS) due largely to the compressive strength and/or the microstructure of the concrete (e.g. stronger bond, confinement effect, etc.), which carried a higher contribution of the axial capacity compared to the timber. This difference is clearly higher comparing the concrete-filled specimens with hollow tubes, which gives

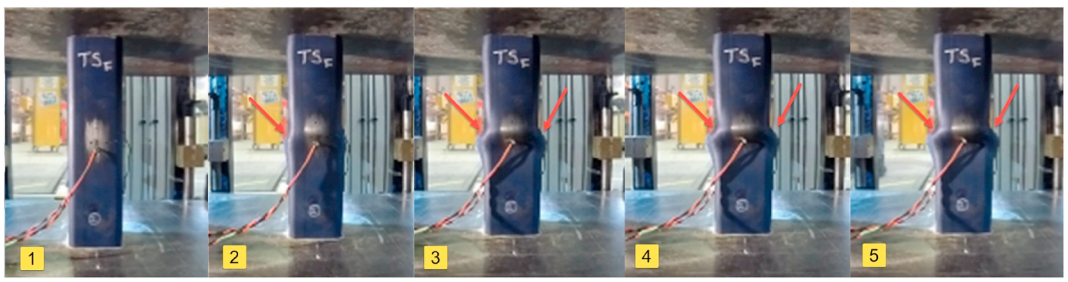

Fig. 5. Failure progress for TS_F specimen.

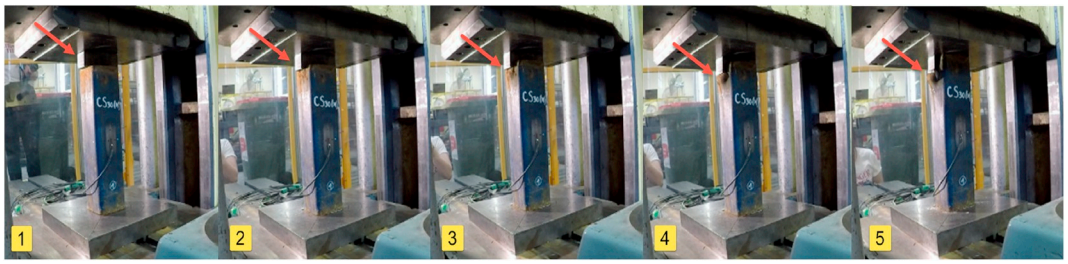

Fig. 6. Failure progress for CS_{30M} specimen.

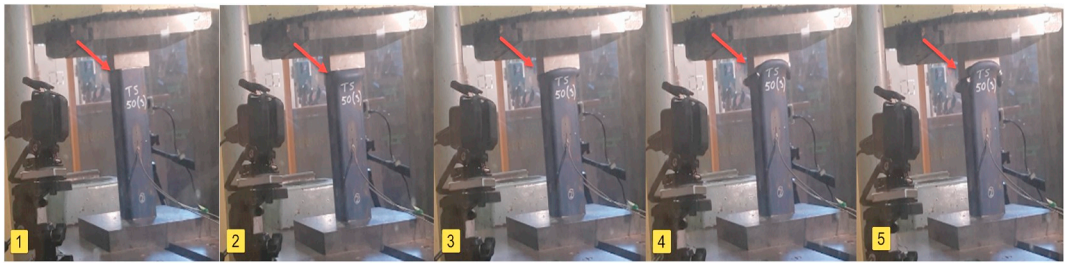

Fig. 7. Failure progress for TS_{50S} specimen.

the average increase of about twofold. Notwithstanding, the difference between fully loaded specimens is quite consistent as timber-filled specimen almost lies between the concrete-filled and the hollow specimens.

Despite the capacity differences, and since mass is critical in many applications such as seismic design, the parameter PLW is the value of peak load divided by the mass. Greater PLW values lead to higher structural efficiency especially for applications that strength-to-mass is a crucial factor in design. Fig. 12-b compares the specimens considering their mass and PLW values. The average PLW values for timber-filled, hollow and concrete-filled specimens are 165.8, 158.8 and 131.5 respectively. This indicates that the average PLW of timber-filled specimens is about 4.4% more than the hollow specimen whilst PLW of concrete-filled specimens is 0.83 of the hollows tubes. So, concrete-filled specimens give high ultimate strengths, but not a higher average PLW value. This suggests a high *structural efficiency* of timber-filled specimens for applications where mass is ineluctable during the design process.

3.4. Absorbed energy, stiffness and ductility

Absorbed Energy (AE) is determined as the area under the axial load-displacement graph [22]. In this research the upper bound at which all specimens can be calculated is assumed 32 mm (Fig. 13-a). The units of the load and the displacement are kN and mm respectively, so AE is measured in Joule. AE values decreased as the area of the loading element became smaller. This indicates that as the loading area approached LCA of 100% (full coverage), the columns were capable of bearing the axial load with full capacity, leading to higher energy absorption. Fig. 13-a ranks the rate of AE as concrete-filled, timber-filled, and hollow steel tubes having the highest, moderate and lowest AE values; this highlights the effectiveness of concrete infill in absorbing energy when confined with steel tubes. Yet timber's contribution was considerable in absorbing energy if compared to the hollow tubes.

Fig. 13-b shows the Specific Absorbed Energy (SAE) of the specimens, which is defined as AE divided by the mass of specimens in grams, so the unit of SAE is J/g. SAE values of hollow, timber-filled and concrete-filled specimens are 6.01, 6.09 and 4.8 respectively, indicating that CFT specimens absorbed lower energy per unit mass.

Two ductility indexes are defined here as *DI* and *DIW* [14]. *DI* is ductility index (Eq. (1)), and *DIW* is ductility index over mass (Eq. (2)). Comparing one index to the other, the variation trend of the results is very similar (Fig. 14), though *DI* magnitudes are over three times greater than *DIW*. This is attributed to the definition of the two indexes as:

$$DI = \frac{\delta_{0.85}}{\delta_y} \tag{1}$$

$$DIW = \frac{DI}{W} \tag{2}$$

in which $\delta_{0.85}$ is the axial shortening at 85% of the peak load in the post-peak region and δ_y is $1.33 \times \delta_{0.75}$ where $\delta_{0.75}$ is the axial shortening at 75% of the axial load in the pre-peak area. The average ductility value of timber-filled tubes is higher than hollow sections, while SAE of the hollow sections was higher than the others. Clearly, this is because SAE is a function of mass, while ductility indexes purely calculate the ductility within a specific range. One of the reasons why the ductility indexes are higher for timber-filled specimens is the higher capacity of these specimens which affects the area under the load-displacement graph, hence the ductility. The concrete-filled specimens were excluded from this comparison because 85% of the peak load in the post-peak zone was not attainable through the load-displacement curves as these specimens manifested a remarkably stable post-yielding trend so the area under the curves is not calculable at the same range as the other groups.

4. Finite element method (FEM)

In order to further investigate the failure mechanism of the tested specimens and also to support the experimental data, three-dimensional finite element models were developed using ABAQUS software [23]. To this end, a combination of steel tubes, concrete/timber cores and rigid plates (Fig. 15-a) were simulated in the same way as the experimental models. The FE models were analysed under full or partial compression until crushing took place.

4.1. Materials

For steel material, the uniaxial stress-strain model with isotropic hardening was adopted based on the average results of the tensile coupon tests (Fig. 4-a). Yield stress, ultimate stress, elastic modulus and

Fig. 8. Failure mode of specimens.

Poisson's ratio of the steel tube are given in Table 1. Concrete was simulated using damage plasticity model; all input parameters are tabulated in Table 4. The Poisson's ratio was taken 0.176 and the modulus of elasticity was calculated using the equation given by American Concrete Institute (ACI) as $4700\sqrt{f_c^{'}}$. Han's model [3] with the following formulas were adopted to achieve and consider the effect of confinement produced by the steel tubes.

$$\xi = \frac{A_s.f_y}{A_c.f_{ck}} = \alpha.\frac{f_y}{f_{ck}} \tag{3}$$

The stress-strain formula for concrete confined with square steel tube equals to:

$$y = 2x - x^2, x \le 1 \tag{4}$$

$$y = \frac{x}{\beta.(x-1)^2 + x}, x > 1 \tag{5}$$

In these equations, $x = \varepsilon/\varepsilon_0$ and $y = \sigma/\sigma_0$.

$$\sigma_0 = \left[1 + \left(-0.0135\xi^2 + 0.1\xi\right) \times \left(\frac{24}{f_c^{'}}\right)^{0.45}\right].f_c^{'} \tag{6}$$

$$\varepsilon_0 = \varepsilon_{cc} + \left[1330 + 760\left(\frac{f_c^{'}}{24} - 1\right)\right].\xi^{0.2} \tag{7}$$

$$\varepsilon_{cc} = 1300 + 12.5 \times f_c^{'} \tag{8}$$

$$\eta = 1.6 + \frac{1.5}{x} \tag{9}$$

The main methodology of this paper is experimental, so FE is a supporting methodology for verification purposes. It is noted that the method presented in Ref. [7] can also be used for confinement in the FE modelling. Thus, it is advisable that the readers consider both methods of Refs. [3,7] for similar simulations and verify the results by available test data. The authors believe that further investigation is required in this area.

To model the tensile behaviour of the concrete, $0.1f_c^{'}$ was calculated considering the slope of linear part used to obtain the modulus of

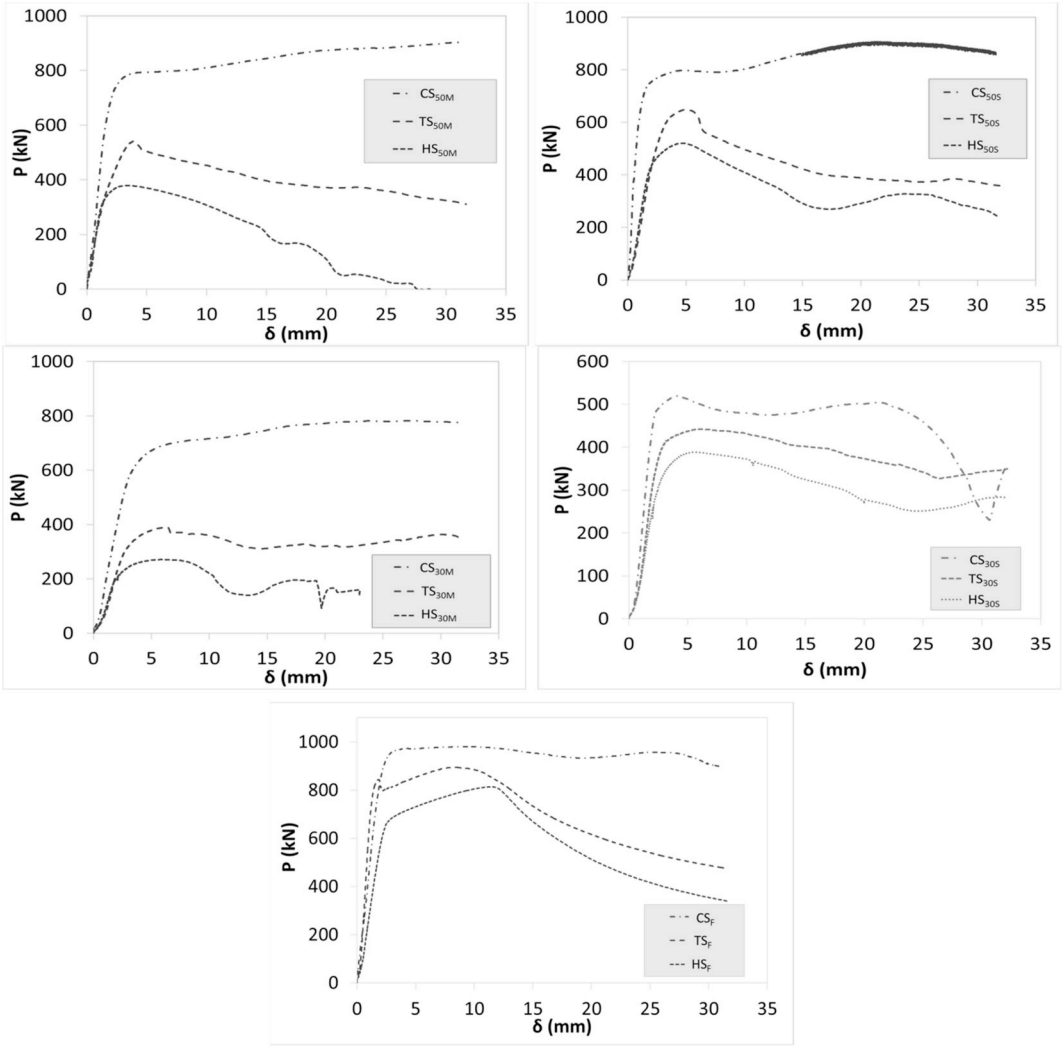

Fig. 9. Axial load versus axial shortening (test data).

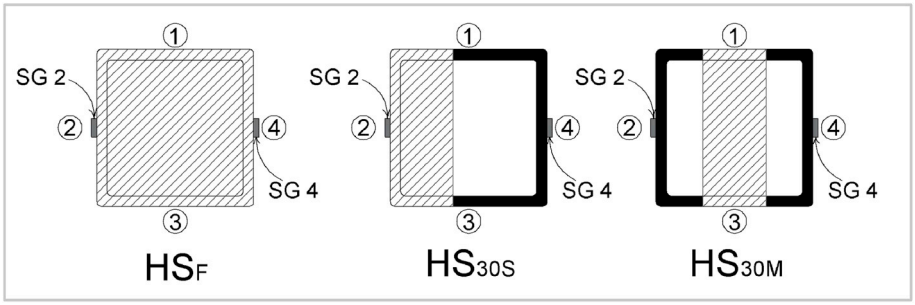

Fig. 10. Strain gauges and their positions on specimens (numbers in circles represent sides of the square).

elasticity. The uniaxial stress-strain model with isotropic hardening behaviour was selected to model the timber material. The Poisson's ratio of timber was 0.3. The modulus of elasticity of timber was considered as the average slope of equivalent stress-strain curves of the timber samples depicted in Fig. 4. The plastic area of timber was modelled as the average values obtained from the four stress-strain graphs out of the material testing.

4.2. Element type, mesh, boundary conditions and analyses

For modelling the three constitutive parts of the composite sections, i.e. steel tubes, concrete and timber core, 8-node solid elements with reduced integration and hourglass control, C3D8R, were employed. Since pure axial deformations of concrete are dominant without any rotation, this element closely reflects the real behaviour of the concrete core [25]. For steel tubes, both shell and solid elements are able to simulate the deformations. However, using C3D8R with proper mesh helps an effective contact and reliable deformations [25]; it also decreases the time of analysis [26] compared to the shell element. So C3D8R solid element was selected for the steel tubes. Using C3D8R element represents the behaviour of timber properly as well. General contact with tangential behaviour was used for the interaction between

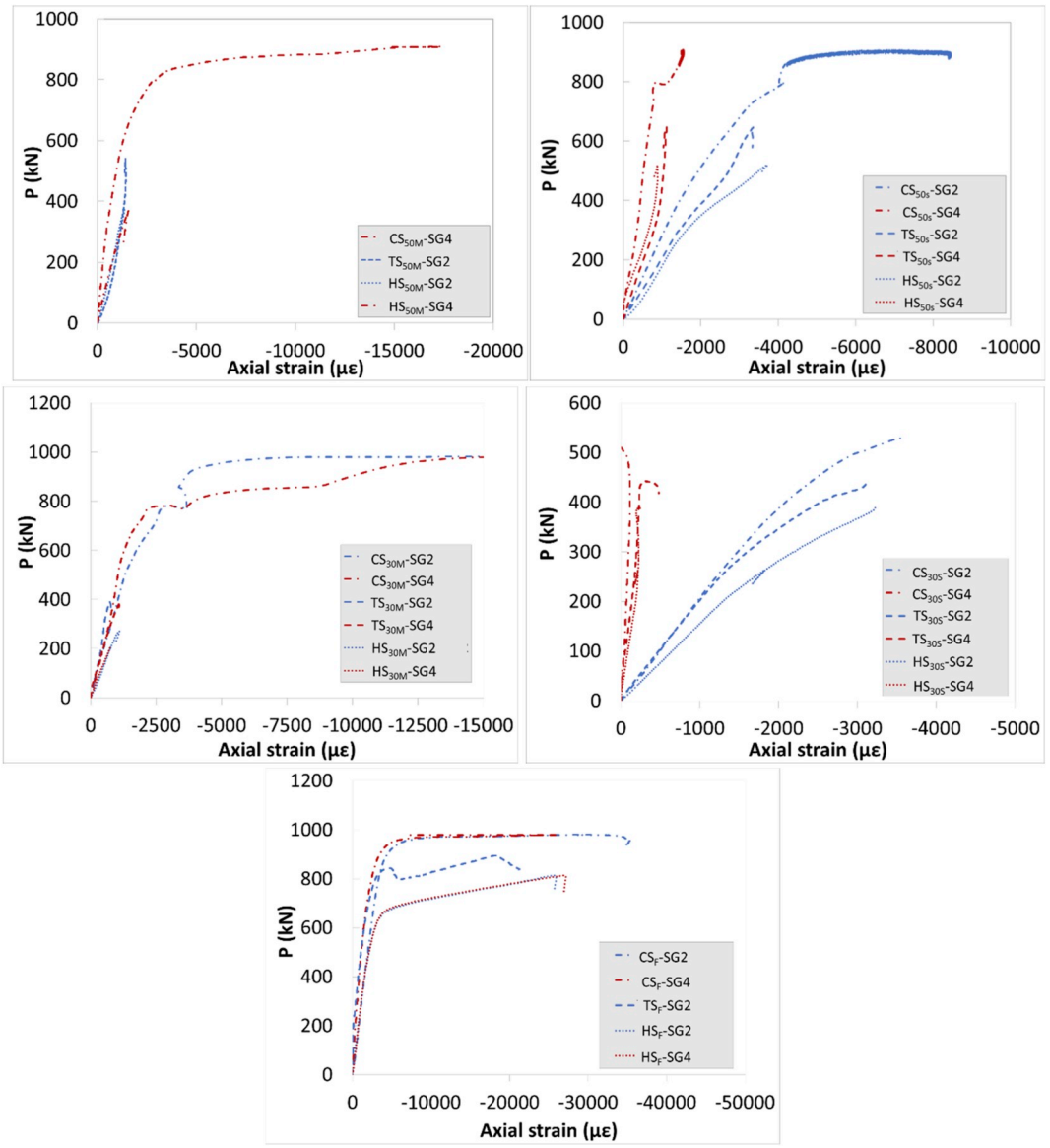

Fig. 11. Axial load versus axial strain.

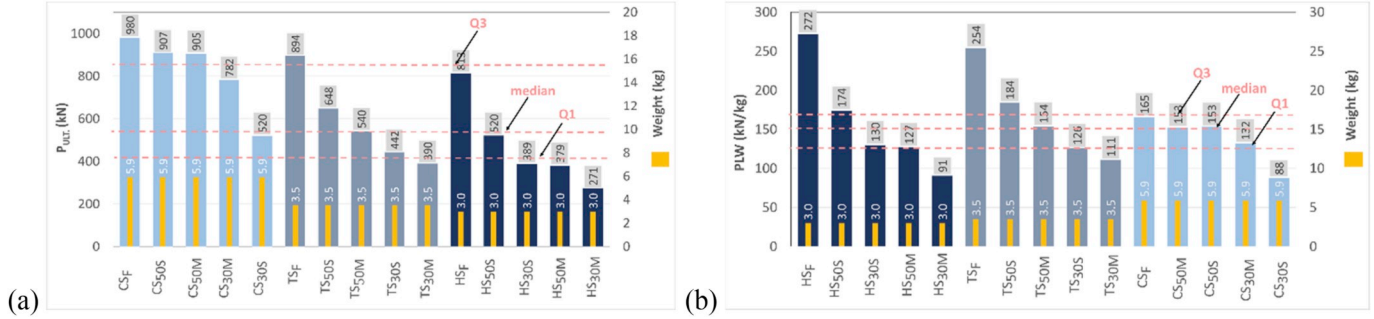

Fig. 12. (a) Peak load for different specimen, (b) ratio of peak load to the total mass.

different components of the composite models including rigid body (loading element) and other materials. Penalty friction formulation with the factor of 0.2 was considered [27], while hard contact was adapted for the normal interactions [28]. For normal interactions, the separation of different components is allowed with no penetration.

A mesh convergence study was conducted to reach a reliable mesh size for these particular composite sections. Several mesh sizes were tried including 2.5, 5 and 10 mm, based on which 5 × 5 × 2.5 mm with the refinement at corners was finally approved for the mesh size of the steel tubes while 5 × 5 × 5 mm was used for the concrete and timber. For rigid plates, elements with 10 × 10 × 10 mm of size were designated. A typical FE model after meshing is shown in Fig. 15-a.

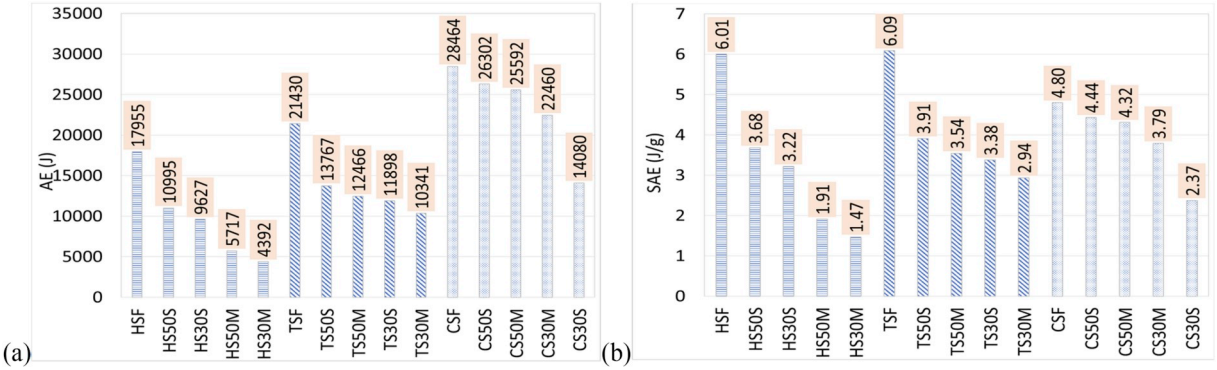

Fig. 13. (a) Absorbed energy (AE), (b) Specific Absorbed Energy (SAE).

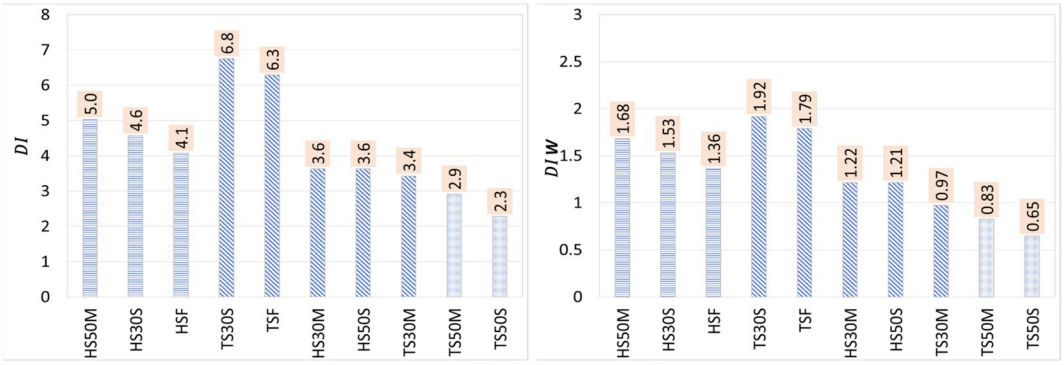

Fig. 14. Ductility indexes *DI* and *DIW*.

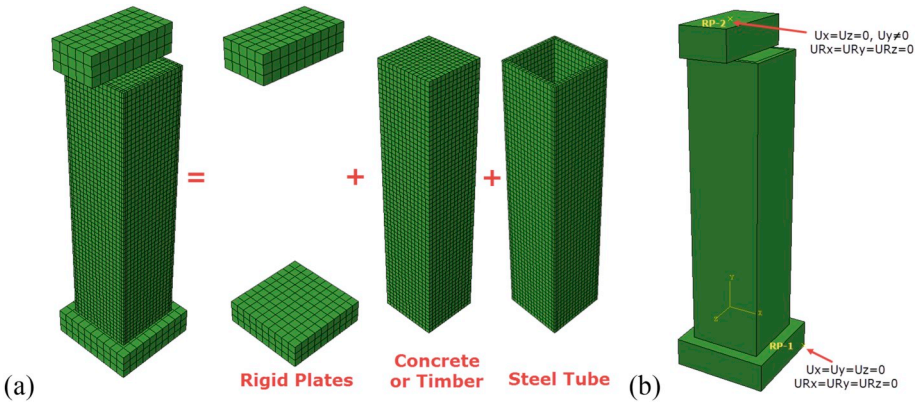

Fig. 15. (a) Different components and meshing, (b) boundary conditions.

Table 4
Damage plasticity parameters [24] (the value of ψ is considered based on tests).

ψ	e	f_{b0}/f_{c0}	K	μ
31°	0.1	1.16	0.6667	0.0002

Two reference points, one at the bottom corner of the bottom rigid plate (RP1) and the other one at the top and centre of the top rigid plate (RP2) were positioned. These reference points then were used to apply the boundary conditions and the axial load. RP1 and RP2 were fixed by restricting displacement and rotation for all directions except for displacement in the longitudinal direction of specimen for RP2 along which the axial compression was applied (Fig. 15-b). Axial load was applied as velocity at the top rigid plate through RP2. The Explicit nonlinear dynamic analysis with quasi-static method was used. In addition to the close consistency of the results of this method compared to the experiments, this analysis overcomes the problems associated with the time of analysis, convergence, and a sizable amount of iterations accompanied with nonlinear static analysis.

4.3. Numerical results and verification

In order to ensure the accuracy of FE modelling, all numerical models were compared with their experimental counterparts. This comparison indicated that the load-displacement response, load carrying capacity and failure modes manifested high consistency of the results of the two modelling methods. Load-displacement curves of FE models and the tested specimens are plotted for ten specimens in Fig. 16. The overall shape of the curves including initial slope (elastic stiffness), yielded

area, plastic hardening/softening, and ultimate axial capacity demonstrates a high level of consistency, and the small differences are in an acceptable range comparing the two methodologies. This difference can be attributed to the non-uniformity of the tested materials, different types of imperfections and so forth. Fig. 17 exhibits a quantitative comparison between peak loads of the numerical and experimental results for all specimens indicating a very good agreement, with the average ratio of P_{FEM}/P_{EXP} equal to 1.03.

Fig. 18 shows the deformed shapes of specimens under axial loading at 30 mm of displacement. This figure classifies the failure modes for partially loaded specimens into two major categories. **(i)** The failure mode for hollow steel tubes and timber-filled steel tubes were generally shear rupture, **(ii)** a combination of shear rupture and bulging was observed for concrete-filled tubes. This can be attributed to the composite action of these materials including the confinement effect of the steel tubes and bond characteristics between the infills and the tubes. For fully-loaded specimens though, local plastic buckling with symmetrically four-sided bulging was seen at different heights (Fig. 18). For the hollow tubes, bulging occurred at top and for the concrete-filled specimens bulging formed at h/3 from the top and bottom. Stress distribution and details of deformations through two longitudinal (side views) and a top view are displayed in Fig. 19. From the top views of CS

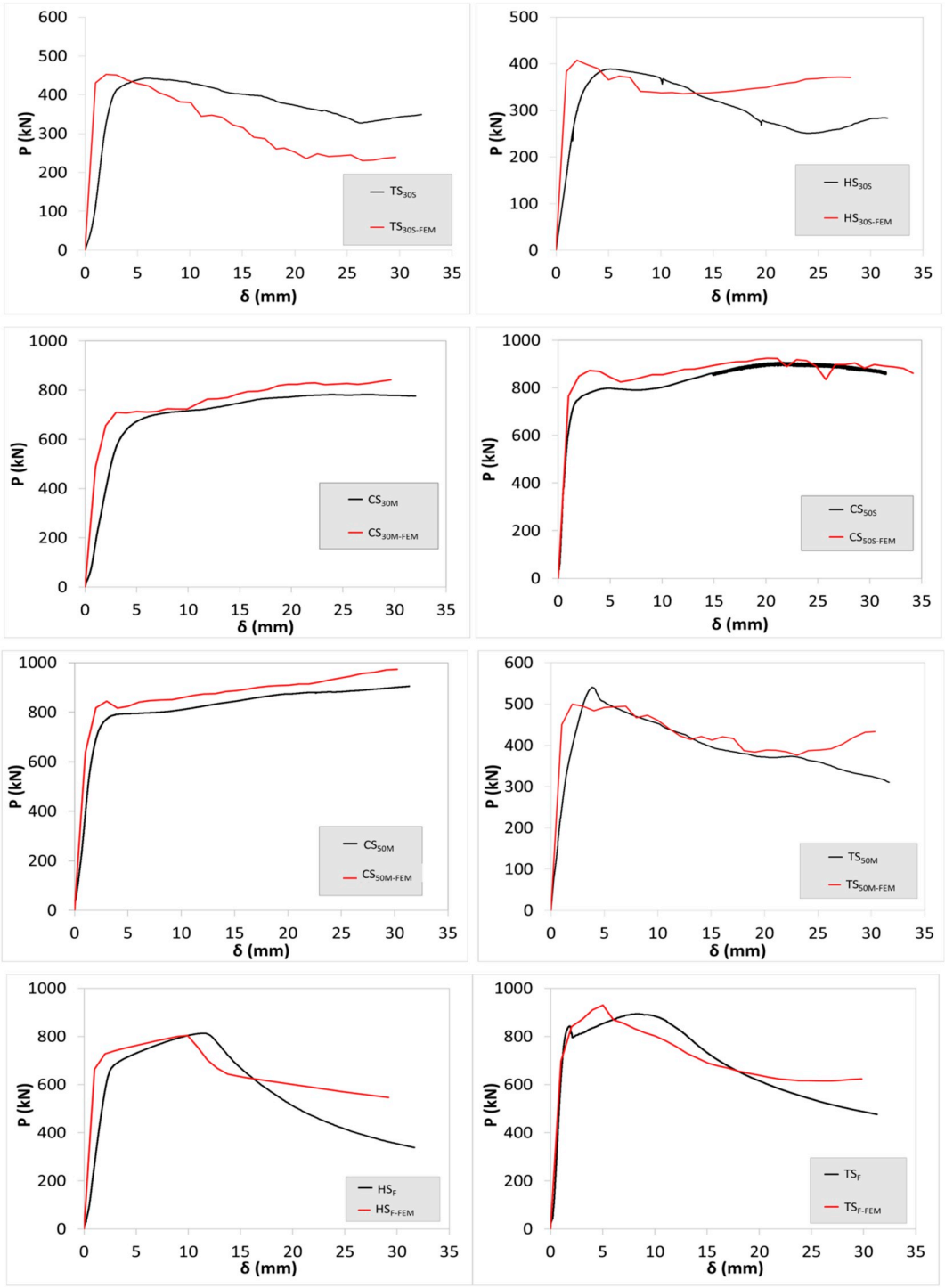

Fig. 16. Comparative axial load-displacement curves for experimental and numerical models.

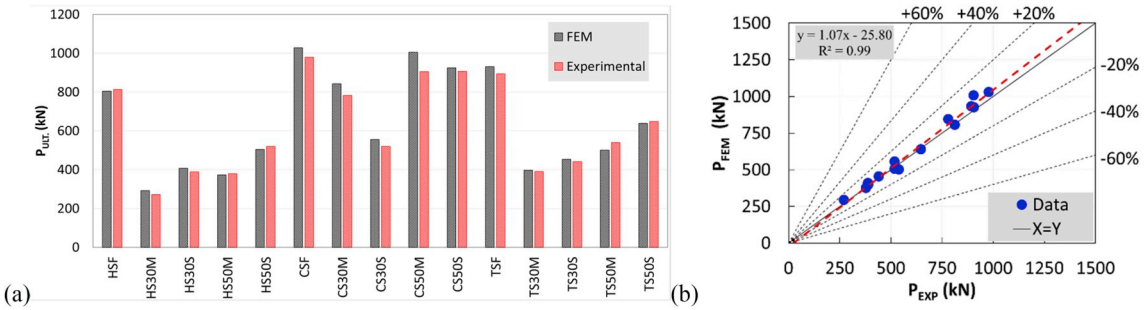

Fig. 17. (a) and (b) Comparison of experimental and FEA results.

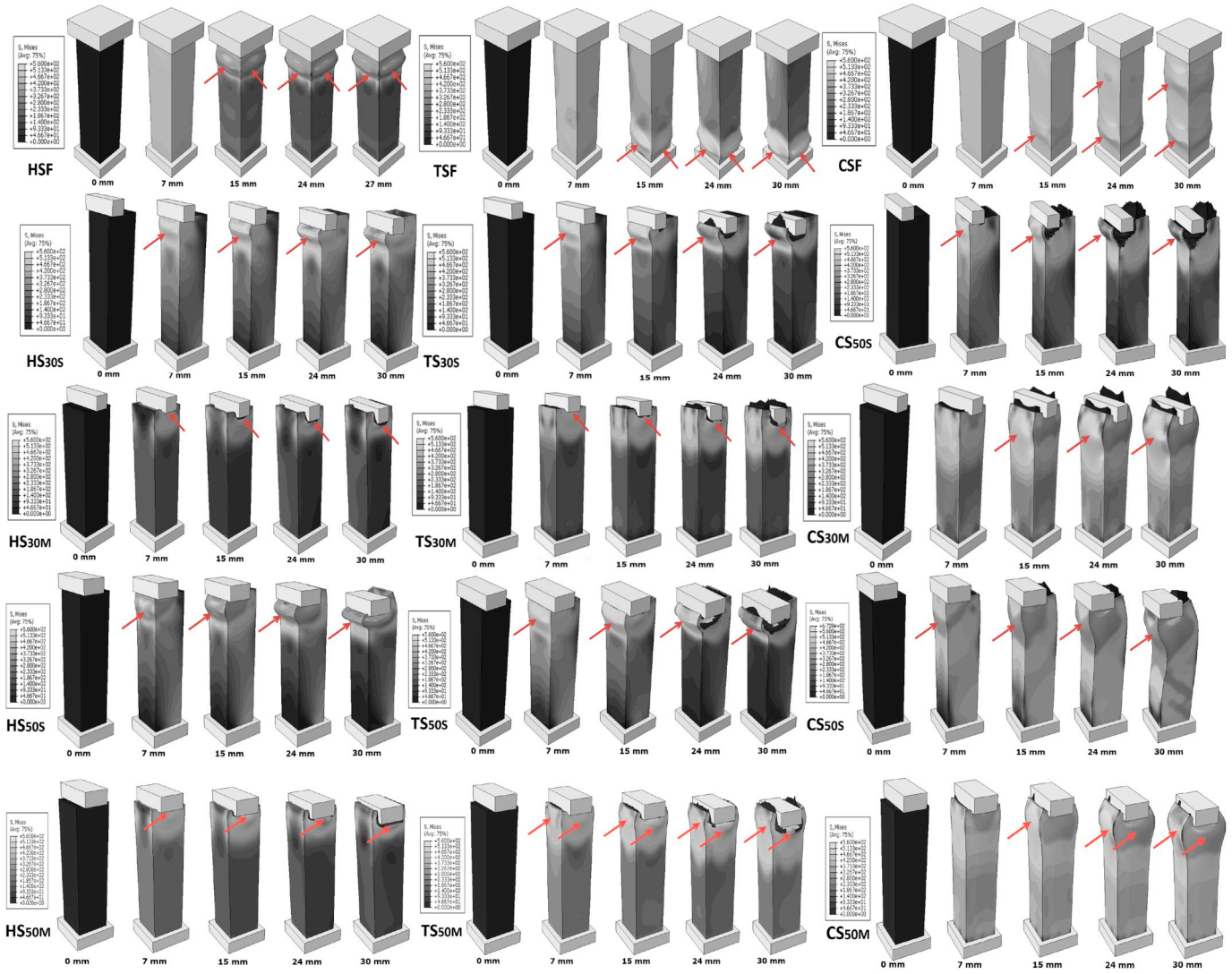

Fig. 18. Progress of deformations and Von-Mises stresses obtained from FEA for all models.

series it is evident that bulging was the dominant failure mode while for other types shear rupture mostly dominated the failure.

5. Conclusion

This paper experimentally and numerically investigates the behaviour of three types of composite sections under three different axial loading conditions. The following results are summarised out of this paper.

1. The failure modes for partially loaded specimens are classified into two major categories. **(i)** Hollow steel tubes and timber-filled steel tubes generally failed in shear rupture, **(ii)** a combination of shear rupture and bulging was observed for concrete-filled tubes. For fully-loaded specimens, the dominant failure mode was plastic buckling as outward bulging.
2. The Specific Absorbed Energy (SAE) and ductility index over mass (DIW) of timber-filled specimens were the highest among all specimens. The average PLW of timber-filled specimens was about 4.4%

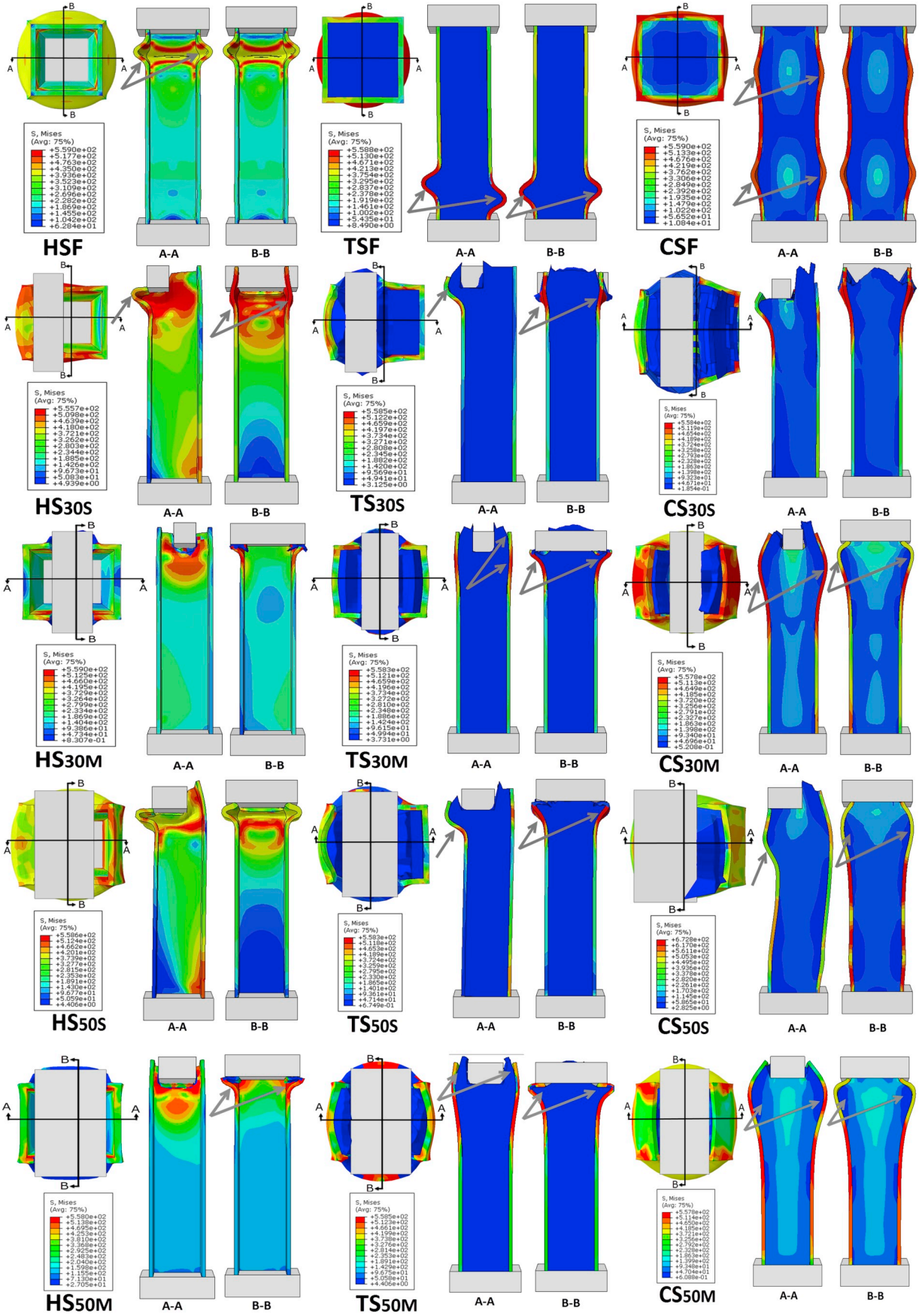

Fig. 19. Axial crushing of the specimens: two longitudinal sections (A-A and B–B) and also the top view.

more than the hollow specimen whilst PLW of concrete-filled specimens is 0.83 of the hollows tubes. So, the concrete-filled specimens gave higher ultimate strengths, but not a higher average PLW value. All these demonstrate the efficiency of these elements when mass is a critical parameter in the design.

3. The concrete-filled tubes experienced higher stability after the yield. Timber-filled and hollow tubes under full LCA had a mild inelastic transition between the yield and the peak load after which the load decreased steadily. For partial LCAs, the load reduction after the peak load was almost similar for hollow and timber-filled specimens.
4. For side-loaded specimens, the failure modes suggest that crushing effectively dominated bending caused by eccentricity. Since the specimens were *stub* columns, the eccentricity could not cause significant bending stress to trigger overall (column) buckling. Additionally, the eccentricity was applied through a relatively short arm. The dominance of the axial deformations to the bending was manifested in the magnitudes of the strains for the side-loaded specimens as SG2 recorded higher values than SG4.
5. Fully loaded specimens had a higher ultimate load than the partially loaded specimens. It is evident that LCA affected the axial stress and the capacity accordingly; as LCA increased, the stress was distributed in a larger area leading to a capacity rise. More importantly though, there is a noticeable capacity difference between the side- and mid-loaded specimens of each group indicating the effect of material under loading. The side-loaded specimens had a higher interface (than mid-loaded) between the loading element and *steel*.
6. Comparing hollow with timber-filled specimens under partial loading, timber increased the capacity for all types of loading up to an average value of 30%. This rise was not as significant as concrete-filled specimens (compared to SHS). This difference was clearly higher comparing the concrete-filled specimens with the hollow tube, which gave the average increase of about twofold.

Acknowledgment

This research was part of the first author's University Research Fellowship at the University of Adelaide. The funding and support of the University are greatly appreciated.

References

[1] G. Ghazijahani Tohid, H. Jiao, D. Holloway, Concrete-filled circular steel tubes with a timber infill under axial compression, J. Struct. Eng. 143 (7) (2017), 04017037, 07/01 2017.
[2] L.H. Han, Tests on stub columns of concrete-filled RHS sections, J. Constr. Steel Res. 58 (3) (2002) 353–372, 03/01/2002.
[3] L.-H. Han, G.-H. Yao, X.-L. Zhao, Tests and calculations for hollow structural steel (HSS) stub columns filled with self-consolidating concrete (SCC), J. Constr. Steel Res. 61 (9) (2005) 1241–1269, 09/01/2005.
[4] Y. Du, Z. Chen, Y. Yu, Behavior of rectangular concrete-filled high-strength steel tubular columns with different aspect ratio, Thin-Walled Struct. 109 (2016) 304–318, 12/01/2016.
[5] A. He, O. Zhao, Experimental and numerical investigations of concrete-filled stainless steel tube stub columns under axial partial compression, J. Constr. Steel Res. 158 (2019) 405–416, 07/01/2019.
[6] L. Guo, S. Zhang, W.-J. Kim, G. Ranzi, Behavior of square hollow steel tubes and steel tubes filled with concrete, Thin-Walled Struct. 45 (12) (2007) 961–973, 12/01/2007.
[7] L.-H. Han, G.-H. Yao, Z. Tao, Performance of concrete-filled thin-walled steel tubes under pure torsion, Thin-Walled Struct. 45 (1) (2007) 24–36, 01/01/2007.
[8] T.Y. Reddy, S.T.S. Al-Hassani, Axial crushing of wood-filled square metal tubes, Int. J. Mech. Sci. 35 (3) (1993) 231–246, 03/01/1993.
[9] T. Ghanbari Ghazijahani, H. Jiao, D. Holloway, Timber filled CFRP jacketed circular steel tubes under axial compression, Constr. Build. Mater. 94 (2015) 791–799, 09/30/2015.
[10] H. Karampour, A. Bismire, B.P. Gilbert, H. Bailleres, Experimental investigation on the structural performance of timber-filled tubular steel stub. World Conference on Timber Engineering, 2018.
[11] T. Ghanbari Ghazijahani, H. Jiao, D. Holloway, Rectangular steel tubes with timber infill and CFRP confinement under compression: Experiments, J. Constr. Steel Res. 114 (2015) 196–203, 11/01/2015.
[12] T. Ghanbari-Ghazijahani, G.A. Magsi, D. Gu, A. Nabati, C.-T.J.E.S. Ng, Double-skin concrete-timber-filled steel columns under compression, Eng. Struct. 200 (2019) 109537.
[13] X.Z.H. Jiao, T.G. Ghazijahani, Capacity of high strength square hollow section steel tube filled with concrete and hardwood timber, in: Tubular Structures XVI: Proceedings of the 16th International Symposium for Tubular Structures, ISTS 2017), Melbourne, Australia, 2017.
[14] A. Nabati, T. Ghanbari-Ghazijahani, C.-T. Ng, CFRP-reinforced Concrete-Filled Steel Tubes with Timber Core under Axial Loading," Composite Structures, 2019, 2019/02/19.
[15] Y.-F. Yang, L.-H. Han, Experiments on rectangular concrete-filled steel tubes loaded axially on a partially stressed cross-sectional area, J. Constr. Steel Res. 65 (8) (2009) 1617–1630, 08/01/2009.
[16] Y.-F. Yang, L.-H. Han, Behaviour of concrete filled steel tubular (CFST) stub columns under eccentric partial compression, Thin-Walled Struct. 49 (2) (2011) 379–395, 02/01/2011.
[17] Y.F. Yang, L.H. Han, Concrete filled steel tube (CFST) columns subjected to concentrically partial compression, Thin-Walled Struct. 50 (1) (2012) 147–156, 01/01/2012.
[18] Y.-F. Yang, L.-H. Han, B.-H. Sun, Experimental behaviour of partially loaded concrete filled double-skin steel tube (CFDST) sections, J. Constr. Steel Res. 71 (2012) 63–73, 04/01/2012.
[19] Y.-B. Zhang, L.-H. Han, W. Li, Analytical behaviour of tapered CFDST stub columns under axially partial compression, J. Constr. Steel Res. 139 (2017) 302–314, 12/01/2017.
[20] W. Li, L.-H. Han, Q.-X. Ren, X.-L. Zhao, Behavior and calculation of tapered CFDST columns under eccentric compression, J. Constr. Steel Res. 83 (2013) 127–136, 04/01/2013.
[21] F. Yuan, H. Huang, M. Chen, Effect of stiffeners on the eccentric compression behaviour of square concrete-filled steel tubular columns, Thin-Walled Struct. 135 (2019) 196–209.
[22] L. Yan, N. Chouw, Crashworthiness characteristics of flax fibre reinforced epoxy tubes for energy absorption application, Mater. Des. 51 (2013) 629–640, 10/01/2013.
[23] ABAQUS-V6.12, "Dassault Systemes," ed.
[24] Y. Du, Z. Chen, M.-X. Xiong, Experimental behavior and design method of rectangular concrete-filled tubular columns using Q460 high-strength steel, Constr. Build. Mater. 125 (2016) 856–872, 10/30/2016.
[25] X. Dai, D. Lam, Numerical modelling of the axial compressive behaviour of short concrete-filled elliptical steel columns, J. Constr. Steel Res. 66 (7) (2010) 931–942, 07/01/2010.
[26] M.F. Hassanein, M. Elchalakani, A. Karrech, V.I. Patel, B. Yang, Behaviour of concrete-filled double-skin short columns under compression through finite element modelling: SHS outer and SHS inner tubes, Structure 14 (2018) 358–375, 06/01/2018.
[27] M. Johansson, K. Gylltoft, Mechanical behavior of circular steel–concrete composite stub columns, J. Struct. Eng. 128 (8) (2002) 1073–1081, 08/01 2002.
[28] H.-J. Lee, H.-G. Park, I.-R. Choi, Compression loading test for concrete-filled tubular columns with high-strength steel slender section, J. Constr. Steel Res. 159 (2019) 507–520.